Dual-Polarization Radar Data Analysis of the Impact of Ground-Based Glaciogenic Seeding on Winter Orographic Clouds. Part II: Convective Clouds

XIAOQIN JING AND BART GEERTS

Department of Atmospheric Science, University of Wyoming, Laramie, Wyoming

(Manuscript received 23 February 2015, in final form 25 July 2015)

ABSTRACT

This second paper of a two-part series aims to explore the ground-based glaciogenic seeding impact on wintertime orographic clouds using an X-band dual-polarization radar. It focuses on three cases with shallow to moderately deep orographic convection that were observed in January–February of 2012 as part of the AgI Seeding Cloud Impact Investigation (ASCII) project over the Sierra Madre in Wyoming. In each of the storms the bulk upstream Froude number exceeded 1, suggesting unblocked flow. Low-level potential instability was present, explaining orographic convection. The clouds contained little supercooled liquid water on account of the low cloud-base temperature. Ice-crystal photography shows that snow mainly grew by diffusion and aggregation. To examine the seeding effect of silver iodide (AgI), five study areas are defined: two target areas and three control areas. Comparisons are made between the control and target areas as well as between a treated, or seeded, period and an untreated period. Low-level reflectivity tends to increase in the target areas relative to the control. This increase is larger in the lee target area than in the upwind target area, suggesting that precipitation enhancement is delayed in the presence of convection. The echo tops of the convective cells are not higher during seeding, relative to simultaneous changes in the control regions. This result suggests that the dynamic-seeding mechanism does not apply for the cold-base convective clouds that are studied here. An analysis of differential reflectivity and snow photography suggests that static seeding is the more likely snow-enhancement mechanism in these clouds.

1. Introduction

Shallow orographic convective clouds may be more suitable for ground-based glaciogenic seeding than stratiform clouds are because the artificial ice nuclei may be mixed over depths exceeding that of the well-mixed boundary layer: convective updrafts may carry these nuclei to higher levels, where they encounter lower temperatures, higher supersaturation values, and a higher supercooled liquid water (SLW) content (e.g., Bruintjes 1999; Pokharel et al. 2015a). In addition, the seeding impact on convective clouds may be enhanced by the extra latent heat released by the freezing of SLW, since this heat release can result in a stronger updraft and a higher cloud top and thus precipitation enhancement (Woodley et al. 1982; Bruintjes 1999; Gagin et al. 1985). Simpson et al. (1967) were the first to test this ''dynamic seeding'' mechanism. Their analysis of 23 randomly selected tropical oceanic cumulus clouds and their numerical simulations showed that seeded clouds tend to have higher tops and more precipitation. This dynamic-seeding mechanism was confirmed later for warm-season cumuli in various environments (Simpson and Woodley 1971; Sax et al. 1979; Hallet 1981; Rosenfeld and Woodley 1989, 1993). Because of the measurement limitations and the challenge to track the seeding-induced microphysical changes in rapidly evolving cumuli, however, these early works focused only on the results (cloud-top height and surface precipitation) rather than on the detailed physical processes. Few of the hypothesized steps in the chain of events of dynamic seeding have been measured in past experiments (Woodley et al. 1982) or have been verified and validated by numerical models (Orville 1996).

The dynamic-seeding mechanism was mainly tested for summertime convection [from cumulus (Cu) congestus to cumulonimbus clouds]. This is because the most important parameter for cloud invigoration by seeding is the amount of extra latent heat—that is, the amount of SLW—and thus the water vapor mixing ratio

Corresponding author address: Xiaoqin Jing, Dept. of Atmospheric Science, University of Wyoming, Laramie, WY 82071.
E-mail: xjing@uwyo.edu

DOI: 10.1175/JAMC-D-15-0056.1

at cloud base. The SLW is much lower in wintertime or cold-based (cloud-base temperature below freezing) convective clouds. For these clouds, the dynamic-seeding concept may be insignificant, and any increase in snow growth may be mainly due to microphysical processes, that is, riming and/or vapor diffusion on ice crystals initiated by artificial ice nuclei in a temperature range within which few natural ice nuclei exist (the ''static seeding'' mechanism). Smith et al. (1984) examine the static-seeding mechanism in high-based cumulus congestus clouds observed over the northern high plains in summer. They assume the hypothesis that the ice crystals produced by seeding preferentially develop into graupel, but the measurements reveal mostly aggregates, possibly because of the lack of SLW in these clouds. They find no evidence of precipitation enhancement by seeding, which they attribute to the lower fall speed of aggregates than that of graupel, thus enhancing evaporation below cloud base. Gagin and Neumann (1981) provide some evidence from data collected in Israel that seeding of convective cold-based clouds can enhance precipitation, although the method and results of this study have been questioned (Rangno and Hobbs 1995). More recent data collected in Israel suggest that, although natural processes are often sufficiently efficient to convert SLW to precipitation, there are occasions with a good potential for precipitation enhancement by glaciogenic seeding of convective clouds (Freud et al. 2015). Other studies have examined the seeding impact on cold-based convective clouds—for example, the Canadian studies by Isaac et al. (1977, 1982), the World Meteorological Organization Precipitation Enhancement Project (World Meteorological Organization 1986; Vali et al. 1988), and Australian experiments (Ryan and King 1997). Most of these studies targeted individual cumulus clouds (rather than a Cu cloud field), and lacked high-resolution radar data.

The study that is presented here examines cases with convective clouds in the 2012 AgI Seeding Cloud Impact Investigation (ASCII-12) campaign, which was conducted over the Sierra Madre in southern Wyoming during January–March of 2012 (Geerts et al. 2013). An overview of weather and cloud characteristics in ASCII can be found in Pokharel and Geerts (2015, manuscript submitted to *J. Appl. Meteor. Climatol.*), and the impact of ground-based seeding on snow growth is analyzed in Pokharel et al. (2015b, manuscript submitted to *J. Appl. Meteor. Climatol.*), using an array of instruments. A recent ASCII-12 case study (Pokharel et al. 2014) examined seeding impact in shallow orographic cumuli, using multiple radars and in situ measurements. Their results show increases in ice-crystal concentrations and in radar reflectivity during seeding, according to three different radar systems, each with different control and target regions. They admit that these changes may have been due to the natural emergence of orographic cumuli during the seeding period, which followed the untreated period. These clouds were hardly present over a control area in the foothills, upwind of the silver iodide (AgI) generators, calling into question the representativeness of such a control area.

Nine good-quality intensive observation periods (IOPs) were conducted in ASCII-12. They were separated into two groups on the basis of radar echo structure (as seen by a scanning radar on the ground) and vertical velocity structure (as seen by a profiling airborne radar). In Jing et al. (2015, hereinafter Part I), we analyzed six mostly stratiform cases. In this paper (Part II) we analyze three IOPs with shallow to moderately deep convection. The objective of this paper is to examine the presence, strength, and location of a seeding signature and to explore the dominant mechanism for seeding cold orographic convective clouds. This study tests two hypotheses: one is that an impact of ground-based seeding on snow size distribution (and thus radar reflectivity) is evident mainly in the lee, rather than at close range, because of the time required for AgI to be lifted in cloud and for snow to fall out in rapidly advecting clouds in these IOPs. The second is that the seeding mechanism is mainly static, and not dynamic, for lack of cloud liquid water.

The analysis method is described in section 2. The ambient weather conditions and storm characteristics are described in section 3. Section 4 explores the seeding effect and mechanisms for snow growth. Section 5 discusses the findings, and the main conclusions are listed in section 6.

2. Analysis method

The topography around the Sierra Madre in Wyoming, along with the locations of the instruments deployed for ASCII-12, is shown in Fig. 1a. The experimental design and instruments are described in Geerts et al. (2013). The main platforms in ASCII-12 are a research aircraft, the University of Wyoming King Air (UWKA), and a Doppler-on-Wheels (DOW) radar. The UWKA carried standard meteorological sensors, a series of particle probes for cloud droplets and snow, and a millimeter-wave profiling Doppler radar—the Wyoming Cloud Radar (Geerts et al. 2010; Pokharel et al. 2014). The main instrument in this study is the dual-polarization scanning X-band DOW radar, located on Battle Pass. This mountain pass, at an elevation of 3034 m MSL, affords excellent low-elevation views toward the upwind (western) and downwind (eastern)

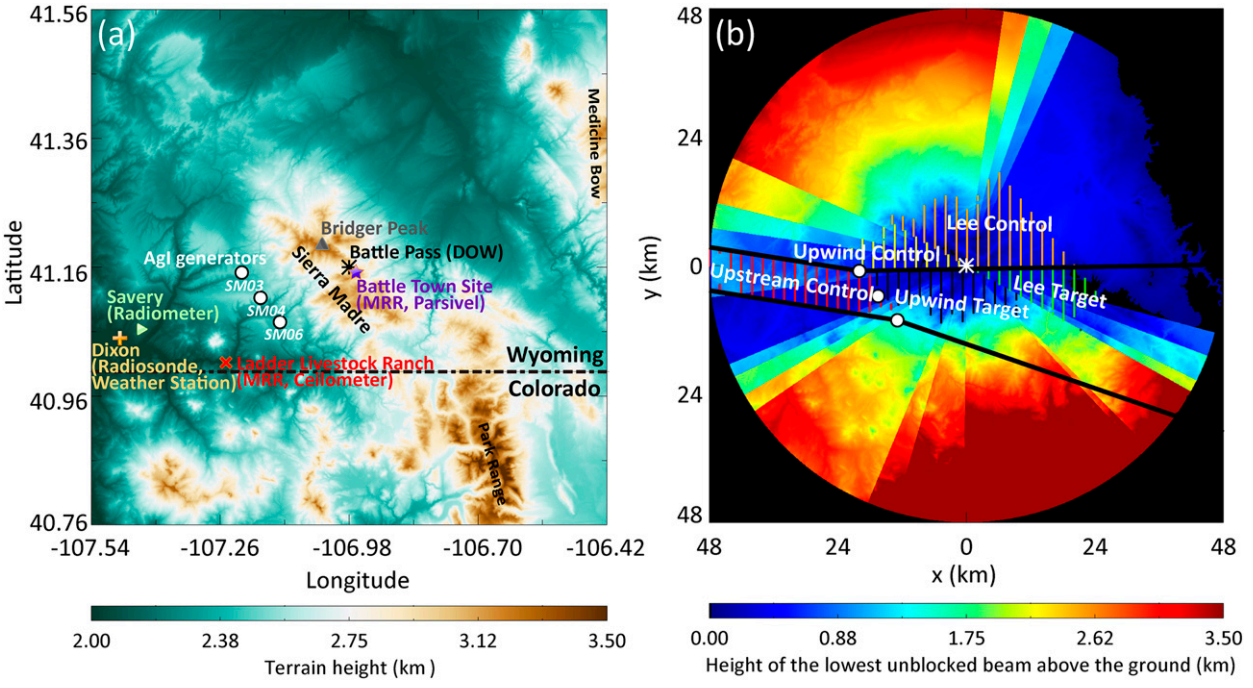

FIG. 1. (a) Terrain map showing the location of the three AgI generators (SM03, SM04, and SM06), the DOW, and other instruments. (b) Height (km AGL) of the lowest unblocked DOW beam. The vertical hatchings show the location of the upstream control (red), upwind control (yellow), upwind target (black), lee control (orange), and lee target (green) areas for IOP8. The black lines upstream of the generators align with the mean wind direction, and those downstream of the generators are rotated out by 10°.

sides of the mountain. The DOW cycled through its scanning strategy every 10 min, starting with a volume scan (lowest elevation angle at −1°) and ending with vertical transects [range–height indicator (RHI) scans] in the direction of the wind. Details of the DOW sampling strategy, data quality control, and further processing can be found in Part I. Here only the analysis method is discussed, with an emphasis on differences with the method used in Part I.

Three areas were defined in Part I to examine the seeding impact, one untreated (the control area, upwind of the AgI generators) and two treated areas, that is, a target area downwind of the AgI generators but upwind of the mountain crest (a fetch of ~18 km) and a second target area farther downwind, in the lee. Here we design a slightly more complicated analysis method involving more representative control areas to capture the terrain-dependent orographic cumulus evolution and to further reduce the impact of natural variability. Orographic convective clouds tend to develop between the foothills and the mountain crest. The upstream control area in the lower foothills may have very few radar echoes, depending on the terrain elevation where convection first emerges in the upslope flow.

Three control areas and two target areas are shown in Fig. 1b, which has the same geographic extent as Fig. 1a but with the elevation of the lowest unblocked DOW beam in the background. The lowest elevation angle (−1°) is unblocked in a narrow window to the west and a broader one to the east-northeast. Battle Pass is surrounded by higher terrain to the northwest and the southeast, and this terrain is cleared only by DOW elevation angles above 3° and 6°, respectively. The five study areas (shown by the vertically hatched parts in Fig. 1b) are designed on the basis of this blockage map. The *upstream control area* (red) is defined as a region that is mostly upstream of the AgI generators where the lowest unblocked DOW beam is no more than 1 km above the terrain. Its eastern boundary is 1 km downstream of the three AgI generators, and its north and south boundaries are determined by the mean low-level wind direction (as measured by radiosondes released from Dixon, Wyoming; Fig. 1a), as shown by the two black lines upstream of the three AgI generators. The *upwind target area* (black) is downstream from the AgI generators but upstream of the mountain crest (the Continental Divide). The *lee target area* (green) is downstream of the AgI generators and the mountain crest but upstream of the downwind valley. The lowest DOW scan is within 500 m of the terrain in both target areas. The target areas are confined to the north and south by black lines in Fig. 1b. These lines run

TABLE 1. Summary of the three IOPs. Shown are the start times (UTC) of the first (''start'') and last (''end'') DOW volume scans included in the NOSEED and SEED periods, the time delay used for certain regions, and the sequence of NOSEED and SEED periods. The duration of each period (h) is shown in parentheses in the NOSEED and SEED columns. The delays are in 10-min increments (the period of the DOW measurement cycle) and are estimated on the basis of the distance from the three AgI generators and the average wind speed shown below in Table 2.

				Delay in start and end of each period (min)			
ASCII IOP	Date	NOSEED start/end	SEED start/end	Upstream control area	Upwind target and upwind control areas	Lee control and lee target areas	Sequence
8	12 Jan 2012	0431/0816 (3.8)	2307/0301 (3.9)	0	20	30	SEED then NOSEED
9	13 Feb 2012	1831/2030 (2.0)	2030/2239 (2.2)	0	20	40	NOSEED then SEED
14	28 Feb 2012	1906/2059 (1.9)	2059/2320 (2.3)	0	10	20	NOSEED then SEED

downstream of the AgI generators and are oriented along the mean wind direction ± 10°. Here, ±10° is used as the AgI plume dispersion angle. This value is narrow, consistent with several observational and modeling studies for low–Froude number (Fr) flows over mountains (e.g., Holroyd et al. 1988; Huggins 2007; Chu et al. 2014). All of this is the same as in Part I.

Here we define two additional areas: the *upwind control area* (yellow hatching in Fig. 1b), located to the side of the upwind target area but otherwise in a similar topographic region, and a *lee control area*, located in the lee of the crest and to the side of the lee target area. This partitioning clearly depends on wind direction and AgI plume-advection patterns, and thus the location and size of the various areas differ from one IOP to another, although in the IOPs examined here the wind direction did not depart much from westerly (section 3a). This design is useful because natural orographic cumulus growth (decay) in the upwind control (lee control) area should be similar to that in the upwind target (lee target) area. Thus a simultaneous comparison between these two areas may reveal a seeding impact. With a beamwidth of 0.93° and an elevation-angle increment of 1°, the DOW's effective vertical resolution at low levels is about 500 m at a range of 30 km (typical for the upstream control area) but 160 m at a range of 10 km (typical for the target areas).

In each IOP, an untreated period (NOSEED) is compared with a treated period (SEED). The NOSEED and SEED periods are ~4 h long in one IOP (IOP8), conducted from late afternoon into the night, and ~2 h in the two other IOPs (IOP9 and IOP14), conducted during daytime hours (Table 1). It is assumed that these sampling periods are long enough to assemble a representative distribution of precipitation echoes in all areas. The advection time through an area is less than 1 h in the worst-case scenario (largest area and least windy IOP). Some time is needed for AgI dispersion and activation; therefore a delay is applied in the target regions that is based on the mean wind speed. This delay is an integral multiple of 10 min, the DOW scan-cycle period. No delay is applied in the upstream control area. SEED preceded NOSEED in IOP8, requiring a buffer period to clear out residual AgI nuclei. We chose this period to be 1.5 h. SEED immediately followed NOSEED in the two other IOPs (Table 1).

First we examine natural changes across the mountain by comparing the various study areas with the upstream control area. The seeding signature, which is superimposed on the orographic effect, will be analyzed by examining the local temporal change (SEED − NOSEED) of reflectivity in all areas. The seeding impact is assessed on the basis of a double difference: the temporal change of reflectivity observed by the DOW in the upwind and lee target areas in comparison with the same temporal change in the upwind and lee control areas. These two control areas are selected as reference because the basic assumption for this double-difference method is that the natural trend in cloud and precipitation properties is the same in the control and target areas (Gabriel 1999).

3. Ambient weather conditions and storm characteristics

a. *Ambient weather conditions*

Three ASCII-12 IOPs were classified as convective (Table 1) on the basis of DOW low-level reflectivity maps and vertical transects of Wyoming Cloud Radar vertical velocity (Geerts et al. 2013). The upstream weather conditions of these three IOPs are summarized in Table 2. The value for N is a weighted average of the dry Brunt–Väisälä (B-V) frequency, calculated between the surface and cloud base [i.e., lifting condensation level (LCL)], and the moist B-V frequency, calculated between the LCL and the height of Bridger Peak, which is the highest point in the Sierra Madre. As expected for

TABLE 2. Summary of the upstream environment for the three IOPs. Temperature T, wind speed, wind direction, the altitude of the LCL, and B-V frequency N are derived from a series of radiosondes released from Dixon (Fig. 1a) during the IOPs. Average values are calculated from three soundings each. The Froude number is calculated as the wind speed divided by the N and the height of Bridger Peak (BP) above Dixon (3354 m). The LWP is inferred from a passive microwave radiometer at Savery. The mean liquid-equivalent snowfall rate S during NOSEED is estimated from an ETI gauge at Battle Town site. The cloud-top temperature (CTT) is derived from the DOW mean echo-top height in the target areas, converted to temperature using radiosonde data.

	700 hPa			LCL		Avg from surface to BP elev				LWP max (mean)		
ASCII IOP	T (°C)	Speed ($m\,s^{-1}$)	Direction (°)	T (°C)	Alt (m MSL)	Speed ($m\,s^{-1}$)	Direction (°)	N ($10^{-2}\,s^{-1}$)	Fr	(10^{-2} mm)	S ($mm\,h^{-1}$)	CTT (°C)
8	−5.9	8.5	277	−3.9	2471	7.7	279	0.52	1.54	32 (2)	0.78	−28
9	−8.2	5.3	249	−4.2	2418	5.1	249	0.32	1.66	8 (3)	0.23	−19
14	−9.1	17.8	288	−6.5	2624	15.3	283	0.27	5.11	23 (7)	0.86	−23

an environment with convective clouds, N is very small in the three IOPs—on average less than $0.5 \times 10^{-2}\,s^{-1}$.

The temperature at the elevation of Battle Pass (~700 hPa)[1] varied from −9.1° to −5.9°C (Table 2). Air passing over Battle Pass thus cooled to at least this temperature before warming in the lee. Parcels of air lifted from the PBL into Cu clouds obviously cooled to lower temperatures that were cold enough for AgI nuclei to initiate ice in cloud (Breed et al. 2014). The low-level wind was roughly westerly in the three cases. The low-level wind was relatively weak in IOP8 and IOP9 ($<8\,m\,s^{-1}$) but was stronger ($15\,m\,s^{-1}$) during IOP14. Nevertheless, given the low stability, the bulk Fr exceeded unity in all cases (Table 2). Therefore the upwind low-level air is expected to be advected across the mountain. The low-level wind direction and the presence of silver in freshly fallen snow (Pokharel et al. 2014, 2015b, manuscript submitted to *J. Appl. Meteor. Climatol.*) at the Battle Town site, located 500 m east of Battle Pass, indicate that the AgI plume from at least one of the AgI generators was advected across Battle Pass during each of the three IOPs (Fig. 1b).

Liquid water was present in all cases in clouds over the Sierra Madre, according to flight-level (not shown) and microwave-radiometer data, although not in large quantities. The average liquid water path (LWP) was below 0.1 mm according to estimates from the radiometer at Savery, Wyoming (Fig. 1a). Hashimoto et al. (2008) and Manton et al. (2011) reckon that LWP values that are larger than 0.2–0.3 mm are required for effective cloud seeding. The LWP trace is variable during the three IOPs studied here, however. The Savery radiometer was pointed toward the Sierra Madre at a low angle just above the horizon. It is presumed that cumulus clouds moved in and out of the radiometer beam. The maximum LWP shown in Table 2 is more representative for the LWP within convective clouds and reached 0.2–0.3 mm, except for IOP9. The cloud-base temperature was approximately −5°C in the three IOPs. The convection was very shallow during IOP9 and IOP14, topping out at ~1 km above Bridger Peak, with cloud-top temperatures around −20°C. At this temperature natural ice nuclei are rare (e.g., Grant and Elliott 1974). Convection was deeper during IOP8, with an estimated echo-top temperature of −28°C.

The key parameter for convective cloud development is static stability, which we investigate by means of profiles of potential temperature θ and equivalent potential temperature θ_e derived from soundings released from Dixon (Fig. 1a). These profiles are shown in Fig. 2 for three soundings during each of the three IOPs. The first two soundings during IOP8 reveal some potential instability in the layer near mountain-crest level (3.0–3.4 km MSL). The air mass in the valley in which Dixon lies is 2–3 K cooler in the third sounding, at 0456 UTC, and not (just) because of nighttime cooling: a weak cold front passed Dixon between the second and third sounding during IOP8, with a surface wind shift to northwesterly at 0443 UTC, according to the Dixon weather station. The frontal inversion was based at 400 m at 0456 UTC and at 700 m in a fourth sounding at 0701 UTC (not shown), with northwesterly wind below this level. Potential temperature profiles above 3.0 km AGL at 0456 and 0701 UTC are similar to those from earlier soundings, with mostly uniform θ_e up to 6.0 km MSL. No clear frontal passage occurred at Battle Pass, although around 0810 UTC there was a slight wind shift and pressure check (not shown). Because the latter time is near the end of the study period (Table 1), IOP8 was not excluded from this study (Geerts et al. 2013).

All three soundings during IOP9 show some potential instability below ~800 m AGL, but the increase of θ_e with height above ~4 km MSL suggests that any convection is shallower than in IOP8. The middle sounding (at 2045 UTC) is least stable. The last sounding (at

[1] The elevation of Battle Pass was within 50 m of the 700-hPa level in the three IOPs.

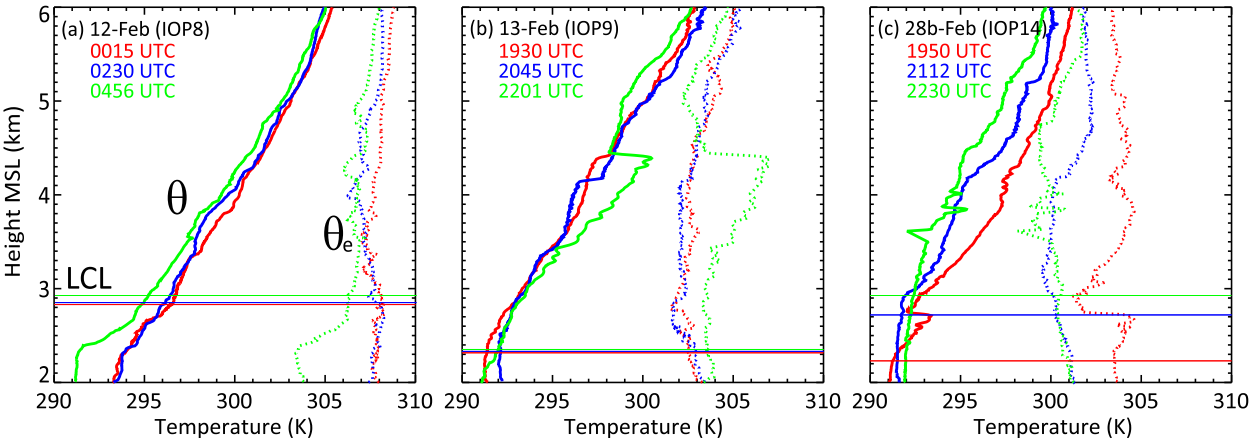

FIG. 2. Vertical profiles of potential temperature θ and equivalent potential temperature θ_e derived from the three soundings for each of the three cases.

2201 UTC) probably ascended within a cumulus cloud because it was saturated up to 4.4 km MSL and showed physically unrealistic absolute instability just above 4.4 km MSL, probably because of cooling by sublimation of rime ice accumulated on the temperature sensor in the radiosonde. The θ profile suggests that this cloud had ~2-K temperature excess (buoyancy) relative to the environment, although the comparison with the other θ profiles is temporal and not spatial. Indeed, buoyancy values up to 2 K were observed at flight level in the penetrated Cu clouds.

All three soundings during IOP14 also show some low-level potential instability. The first sounding has a higher θ_e in the boundary layer than the two others, not because it is warmer but because it has surplus water vapor. This first sounding suggests that convection is suppressed by relatively warm air above the boundary layer, whereas in fact convection was present at this time (Fig. 3c), albeit shallow.

In summary, the θ and θ_e profiles during these three IOPs generally show some potential instability across the LCL, which is favorable for the initiation of convection upon layer lifting. This convection is benign: in none of the soundings does CAPE exceed 100 J kg^{-1}. In all cases the potential instability (or quasi neutrality) is shallow, starting at a level below the height of the AgI generators (2.47 km on average). Thus the convection is coupled with the surface, and AgI nuclei released by ground-based generators can mix into the convective clouds.

b. *Storm characteristics*

The basic storm characteristics are illustrated in Fig. 3 with DOW RHI scans of reflectivity. The echo tops were highest during IOP8 (Fig. 3a), ~3 km above DOW level (ADL), although intense echoes (say, >20 dBZ) topped at a level only one-half as high. Convection was present over the Sierra Madre throughout the IOP, sometimes persisting across the downwind valley (Fig. 3a). Convection was more intense and deeper during SEED (Fig. 3d), in the late afternoon, with the 20-dBZ echo top reaching up to ~2 km ADL and weaker cells reaching up to ~5 km ADL.

IOP9, which is explored in detail by Pokharel et al. (2014), was a postfrontal case with equally persistent but shallower convection, topping below ~1 km ADL (Fig. 3b). The convective echoes were small but intense throughout the IOP and were confined to the Sierra Madre more than in the other two IOPs. No significant changes occurred from NOSEED to SEED, although an average low-level reflectivity-difference map for this IOP shows a slight strengthening in most areas.

IOP14 had shallow, weakly precipitating orographic cumuli (Fig. 3c) in a very cold northwesterly postfrontal airmass. The strong winds in this IOP confined the echoes mostly to the upwind side. Precipitation rapidly dissipated on the lee side, probably because of plunging flow, which was observed by airborne radar (not shown). Convection was actually more intense over the Medicine Bow range to the northeast (Fig. 1a) during this IOP. Convection upwind of the Sierra Madre weakened slightly from NOSEED to SEED; otherwise no significant changes occurred.

4. Exploring a seeding signature

a. *Natural evolution of shallow convection across the Sierra Madre*

For ground-based seeding to have an effect on convective clouds, the clouds must have their roots in the

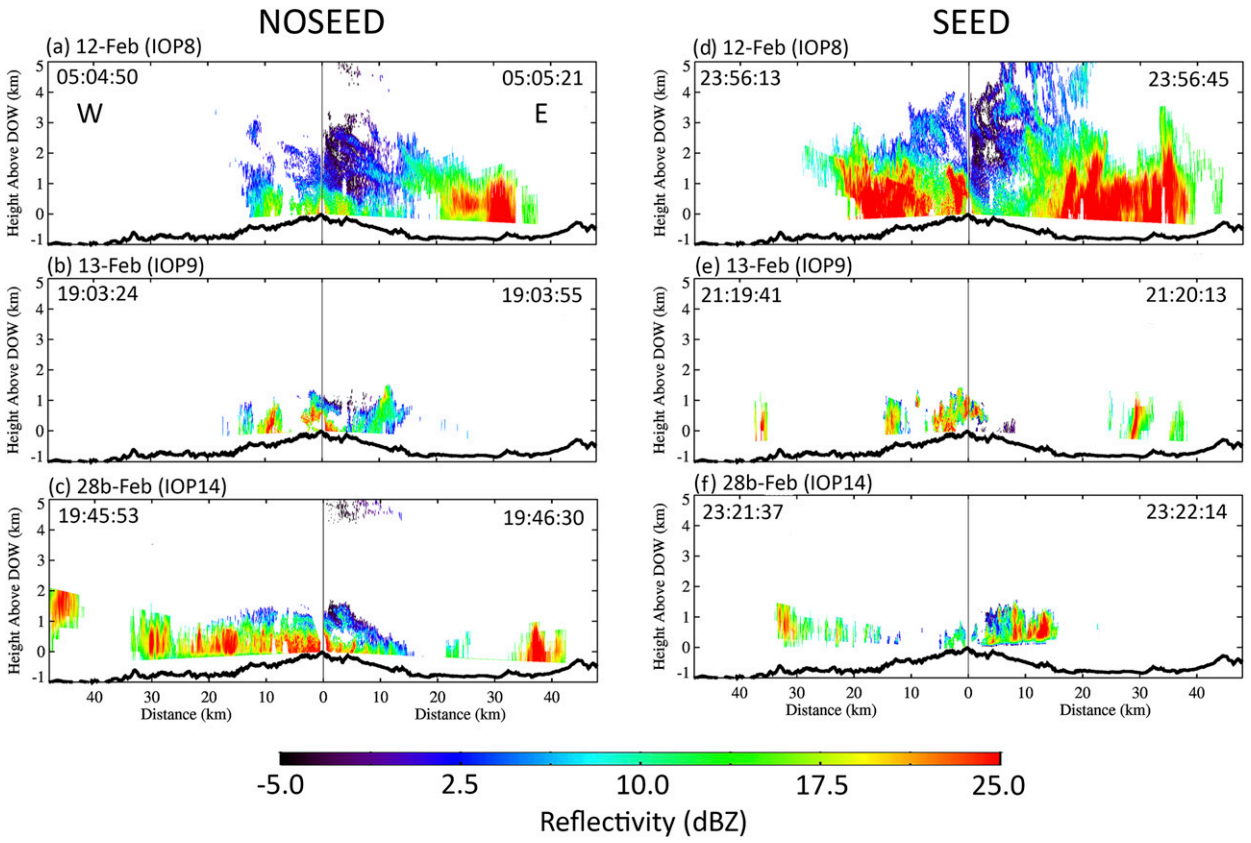

FIG. 3. RHI-scan examples of reflectivity for the three cases during the NOSEED and SEED periods. They are oriented approximately along the wind from west (left side of panels) to east (right side of panels).

PBL downstream of the AgI generators (Gagin et al. 1985), that is, between the foothills and the mountain crest. Therefore we first examine how the echoes developed in natural conditions during SEED. Figure 4 shows four consecutive (10-min separation) base-reflectivity images for each of the three IOPs. The tracing of cells with time illustrates how the convection evolved. In IOP8 convective echoes were embedded in widespread weak echoes. They maintained their strength as they traveled through the domain, which suggests that they are long-lived and little affected by the underlying terrain (Fig. 4a). In IOP9, echoes were more isolated and started fairly far upwind, often upwind of the generators. Numerous small cells reached their peak strength upwind of or at the crest and dissipated over the lee valley (Figs. 4b and 3b). In IOP14 convection was also mostly confined to the upwind side, often starting upwind of the generators, but the cells were weaker. There was no 0° plan position indicator (PPI) scan at ~2322 UTC; hence the last panel is 10 min later.

In short, Fig. 4 suggests that at least some of the cells grew or emerged between the AgI generators and the crest. Therefore we can explore a seeding signature. First we investigate how convective clouds develop as they move from the foothills (upstream control area) to the region upwind of the crest and to the leeside. Figure 5 shows the reflectivity frequency-by-altitude diagrams (FADs; Yuter and Houze 1995) of the five study areas (Fig. 1b) during the NOSEED period, for the three IOPs combined. The reflectivity-difference FAD, relative to the upstream control area, is also shown in Fig. 5 for each area.

The FADs describe the DOW reflectivity frequency distributions above ground level (AGL). Ground level is considered as the reference level because the depth of the boundary layer and isentropes generally follow the terrain. In all FADs, the vertical resolution is 100 m and the horizontal resolution is 0.5 dBZ. The count in any bin is normalized by the total count at that particular level AGL, as in Part I. This method, unlike the 2D normalization used in other studies (e.g., Geerts et al. 2010), keeps the reflectivity distribution at a certain level unaffected by that at other levels, and therefore precipitation changes near the surface can be examined without any influence from

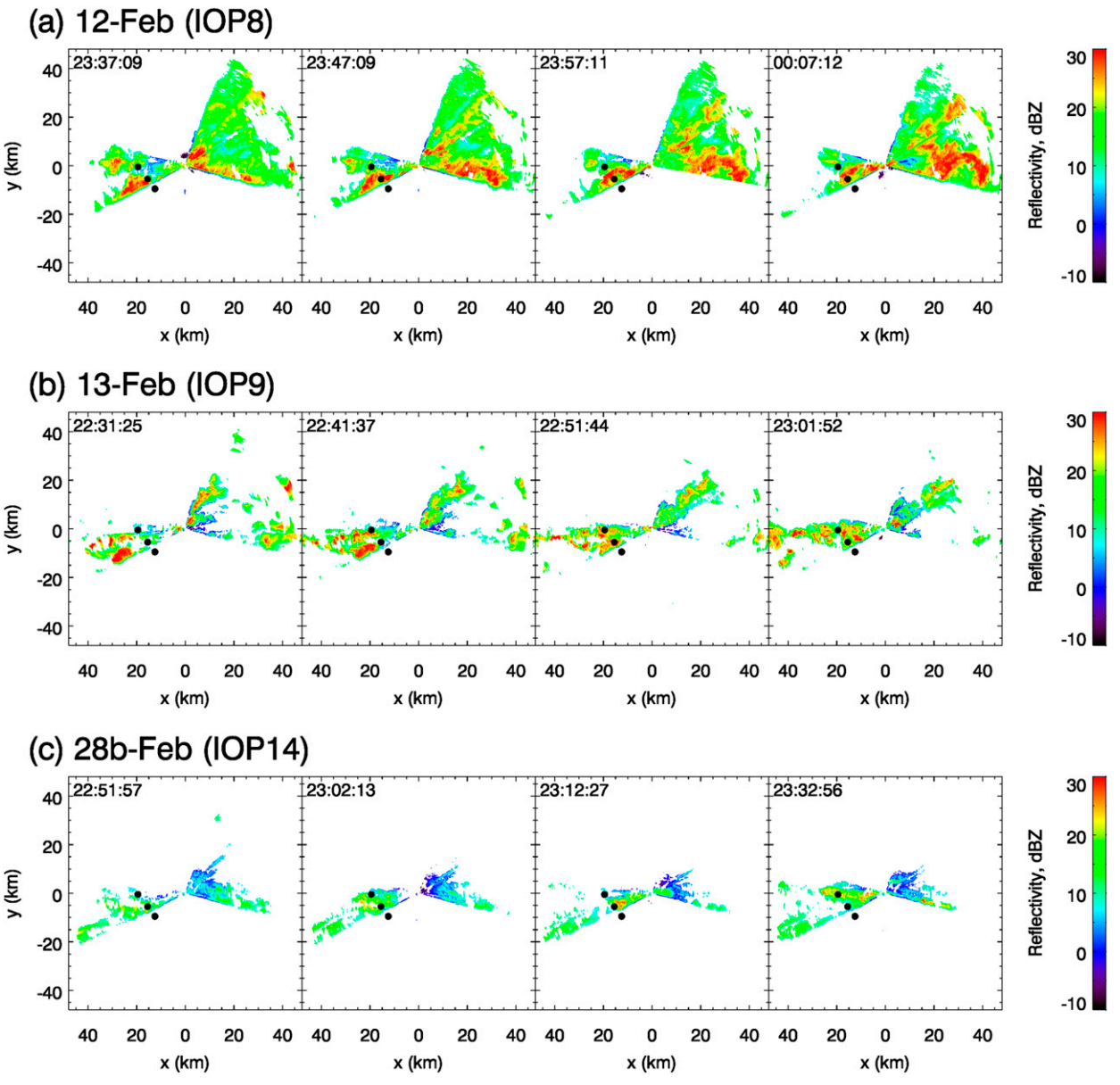

FIG. 4. Examples of PPI scans at 0° elevation for the three cases, all during SEED. The black dots indicate the locations of the AgI generators. The domain is the same as in Fig. 1.

echo changes aloft. The drawback of this 1D-normalization method is that it emphasizes the frequencies at levels at which few echoes exist, for example, near cloud top. Therefore, awareness of the data presence at each level is important. This presence is expressed as a fraction ranging between 0% and 100% (yellow line in Fig. 5).

The positively skewed reflectivity distribution in all regions (Fig. 5) is typical of shallow orographic convection: strong echoes occupy little area, whereas weak echoes are widespread because (mostly convectively generated) snow particles survive in interstitial shallow stratiform cloud because of airmass lifting above the LCL; thus the convective cells are embedded in weak stratiform precipitation (Fig. 4). The mean reflectivity (white lines in Fig. 5) is representative of convective precipitation, however, since the mean is computed in units of reflectivity Z ($\mathrm{mm^6\,m^{-3}}$) and not reflectivity decibels (dBZ). (Echo-free areas are not counted in the average.) Note that snowfall rate S is proportional to Z^b, where constant b is approximately 0.67 (Matrosov et al. 2009). Thus the linear dBZ scale in the abscissa of

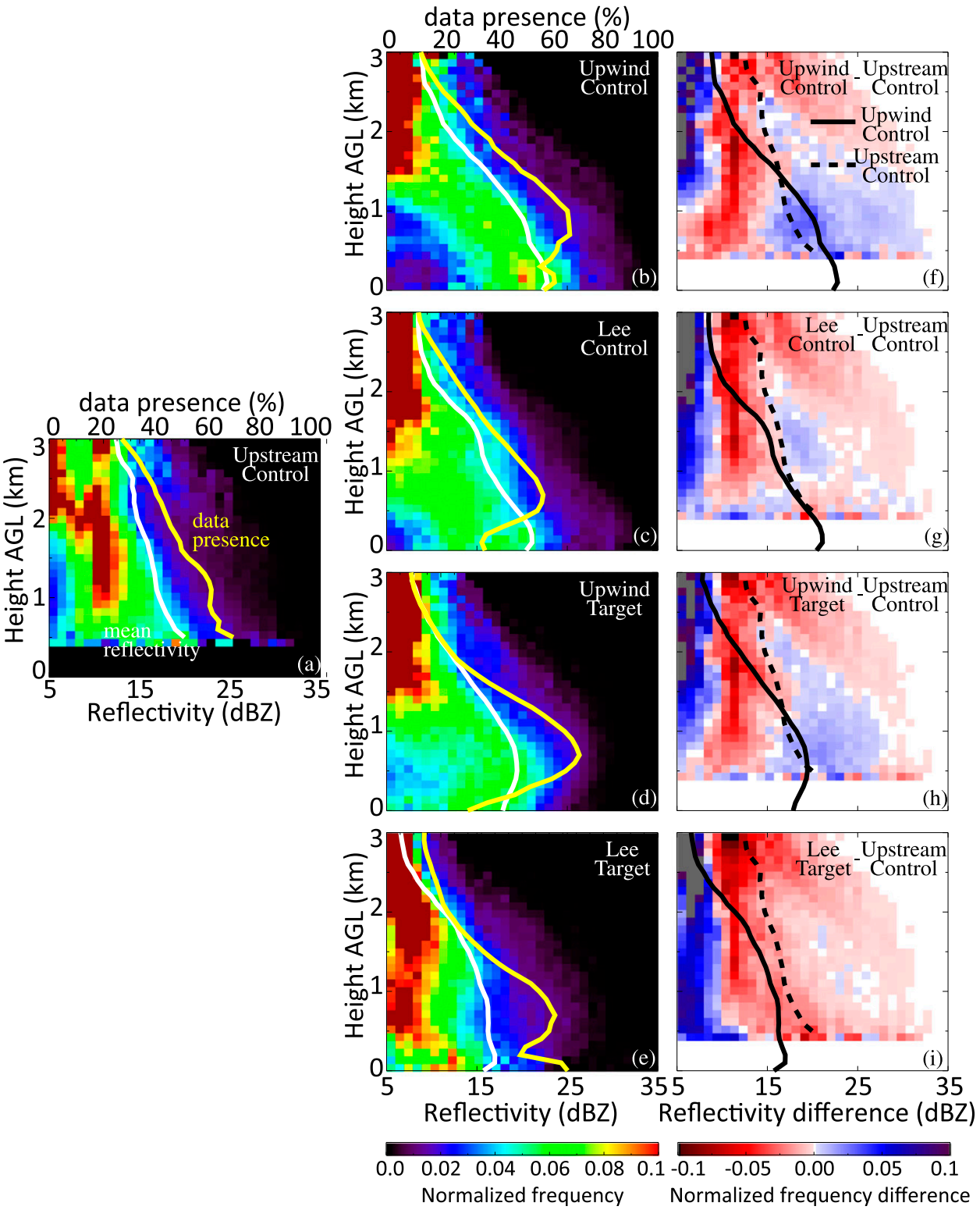

FIG. 5. Composite DOW (a)–(e) reflectivity FADs of the five study areas during NOSEED, along with reflectivity-*difference* FADs: (f) upwind control − upstream control, (g) lee control − upstream control, (h) upwind target − upstream control, and (i) lee target − upstream control. The average reflectivity profiles are shown as white lines in the FADs and as black lines in the difference FADs. The data-presence profiles are shown as yellow lines in the FADs.

all panels in Fig. 5 corresponds to an exponential increase in snowfall rate.

Natural orographic precipitation enhancement is evident in Fig. 5: Z values at low levels (lowest 1.0–1.5 km AGL) increase from the foothills (i.e., the upstream control area) to the region just windward of the crest (upwind control and target areas; Figs. 5f,h). Low-level reflectivity values decrease rapidly across the crest as convective cells dissipate on the lee side (lee control and target areas), and snow falling below cloud base sublimates (Figs. 5g,i). In general, low-level Z values are highest windward of the crest, are intermediate in the upstream foothills, and are lowest in the lee. The highest echo tops (relative to ground level) tend to occur in the foothills, suggesting that some convective cells had already matured there, and the equilibrium level did not rise over the terrain as much as the terrain itself. This is a common feature for the three IOPs during the NOSEED period and, to a lesser extent, during SEED as well (Fig. 6), although the echo strengths and depths were different in the three IOPs. This justifies the compositing of the three IOPs into a single FAD.

There is little difference in the evolution of low-level Z from the foothills to the upwind and lee control areas during SEED (Figs. 6f,g). The same relation can be expected in the upwind and lee target areas if AgI seeding has no impact on the cloud and precipitation, but low-level reflectivity does *not* decrease from the upwind target to the lee target area during SEED (Figs. 6h,i). This will be explored next.

b. Changes in reflectivity profiles during seeding

We now investigate the temporal reflectivity change (SEED − NOSEED) in each of the five study areas by means of Z-difference FADs, again composited for the three IOPs (Fig. 7). At first glance a red–blue (left–right) dipole dominates across the entire region, at all levels, suggesting that storms were stronger and deeper during SEED. This is due to natural changes observed mainly in IOP8, and also IOP9 (section 3b). The temporal changes aloft (above 1–2 km AGL) are similar in the pair of adjacent areas upwind of the crest (Figs. 7b,d), and in the pair of areas in the lee (Figs. 7c,e). There are some more subtle differences between the three control areas and the two target areas, however. In the upstream control area, the mean Z profiles are similar in the NOSEED and SEED periods. In the upwind and lee *control* areas, red (blue) dominates on the right (left) side below ~0.5–1.0 km AGL. This means that low-level reflectivity was slightly smaller during SEED, even though echo-top heights generally were higher.

Yet in the two *target* areas, especially the lee target area, the low-level Z-difference dipole is reversed, with blue dominating on the right. Thus, while the control areas suggest little change in Z profiles (echo-top increase yet a slight orographic precipitation decrease) from NOSEED to SEED, *low-level reflectivity is enhanced in the target areas, especially at larger fetch*, in the lee. This result probably implies more surface snowfall, given the availability of Z measurements very close to the ground at close radar range. This increase in mean low-level Z in the target area, relative to the natural change in the control areas, may be a seeding signature. It is clear that the composite FAD and mean Z values are dominated by the most intense storm, that is, IOP8, but all three IOPs are very similar in that they show this increase, as will be shown later.

c. Changes in echo-top height during seeding

To explore the possibility of a dynamic-seeding mechanism (Cu top deepening), we examine the mean values of the 5- and 20-dBZ echo-top height change (SEED − NOSEED; Fig. 8). The 5- and 20-dBZ thresholds are chosen to present the precipitating-cloud top and convective-core top, respectively. We show both the average height as based on all 5-dBZ echo tops and that as based on the upper 10th percentile of 5-dBZ echo tops. The former is biased toward the interstitial, mostly light stratiform precipitation, whereas the latter is intended to isolate the convective towers penetrating above this precipitation. The same distinction is made for the 20-dBZ core depth, to distinguish between all convective cores and the deepest (tallest) cores. The DOW volume scans are well suited for this analysis because coverage aloft is better than at low levels (Fig. 1b), especially in the control areas, although at large range the spatial resolution deteriorates.

The 5-dBZ cloud-top height and 20-dBZ echo-core depth are larger during SEED in IOP8 because of some deep, large cells (Fig. 3d), but the increment in these heights is not larger in the target areas than that in the control areas (Figs. 8a,d). IOP9 and IOP14 were dominated by steady shallow convection throughout the IOPs. They too do not reveal any 5-dBZ cloud-top height increase in the target areas (relative to the control areas) during seeding (Figs. 8b,c). The 20-dBZ echo cores were very small in these cases (Fig. 3), especially for IOP14, and again these cores did not deepen during seeding in the target areas relative to the control areas (Figs. 8e,f). We tried several other possible reflectivity thresholds to identify cloud top (e.g., 0 dBZ) and convective-core top (e.g., 15 dBZ). They show similar results for all three IOPs. Thus the cases examined here *do not support the dynamic-seeding mechanism in cold-base shallow orographic cumuli:* glaciogenic seeding does not raise the height of Cu echo tops.

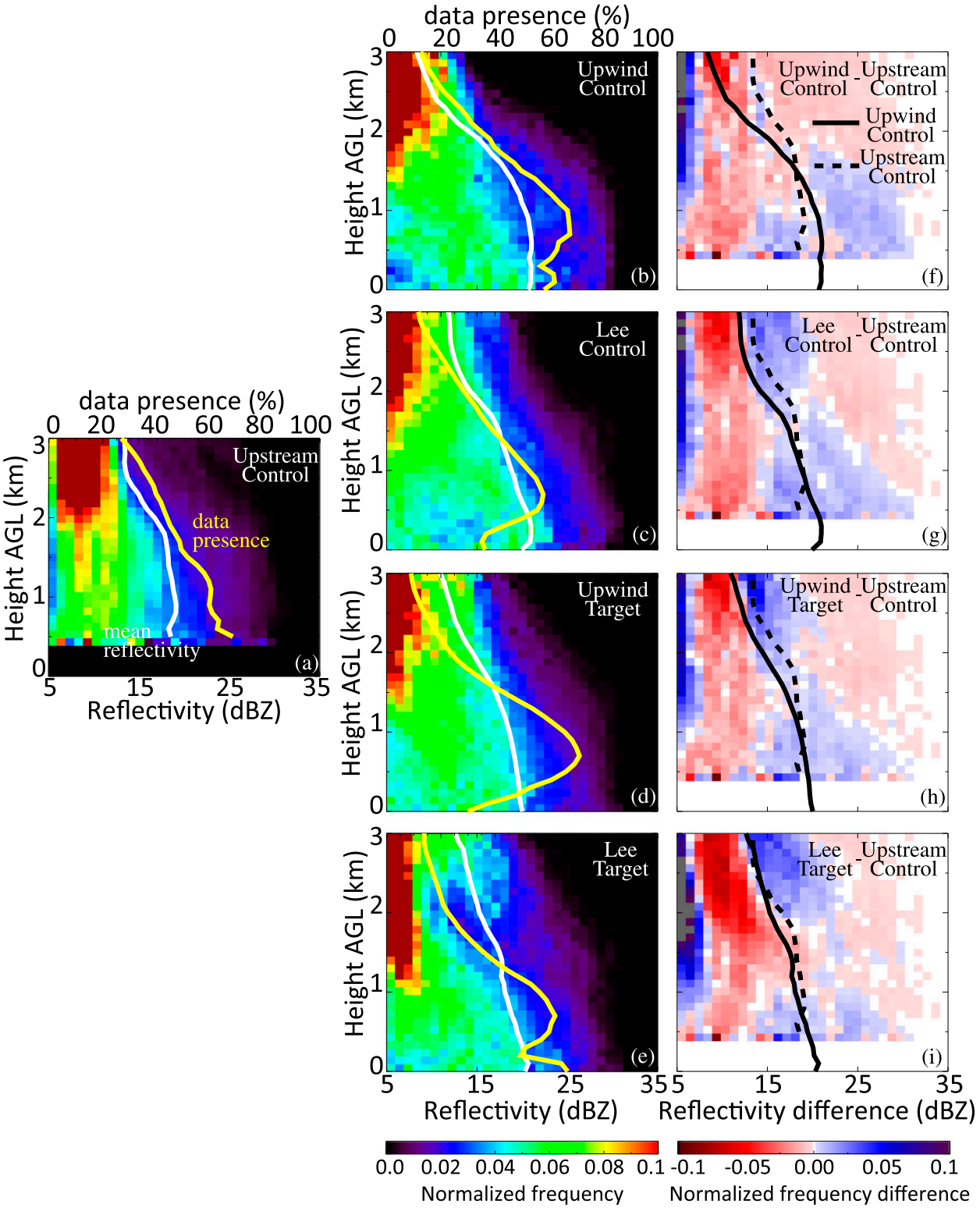

FIG. 6. As in Fig. 5, but for SEED.

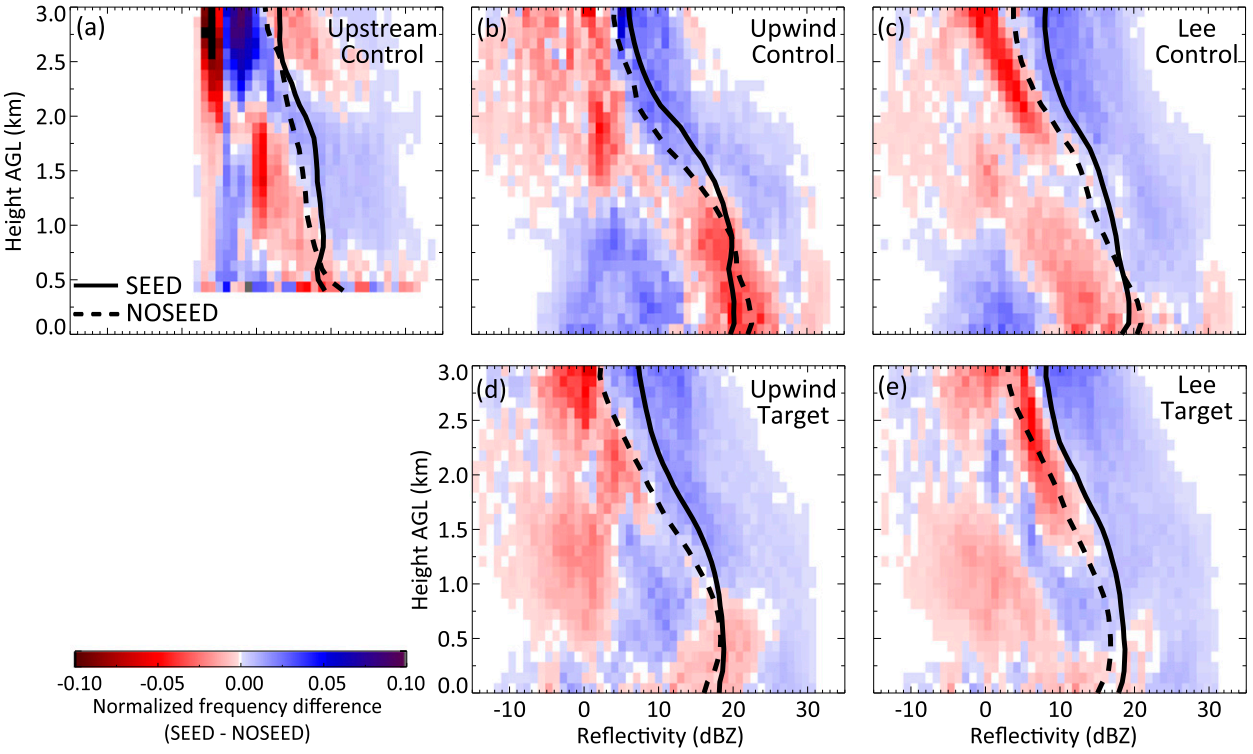

FIG. 7. Composite reflectivity-difference FADs for the three cases for the five study areas. Here the difference is temporal (SEED − NOSEED). The average reflectivity profiles during NOSEED (SEED) are shown as dashed (solid) black lines.

d. Changes in convective-core strength during seeding

To examine how the precipitation may change within the convective cores, we plot the mean profiles of the upper 10th percentile of reflectivity (Fig. 9). Mountain-scale trends are evident in Fig. 9: from NOSEED to SEED periods, convective cores intensified in IOP8 and IOP9 and weakened in IOP14. These temporal changes are substantial. The low-level reflectivity was larger in the lateral control areas (upwind and lee control; solid lines in Fig. 9) than in the corresponding target areas (upwind and lee target; dashed lines) in all three IOPs during NOSEED, possibly because the mountain crest is higher to the northwest and southeast of Battle Pass.

This situation changes during SEED, however. The low-level reflectivity in the convective cores is about the same in the target areas as in the control areas during SEED in IOP8 rather than being less. This result may be due to natural variability: the upper-level reflectivity is larger in the target areas during SEED (Fig. 9b). The DOW RHI scans reveal some stronger convective cells during SEED (Fig. 3d). The low-level reflectivity in the two target areas is slightly larger than those in the two control areas in IOP14 (Fig. 9f). Reflectivity continues to increase toward the ground in the target areas but not in the control areas in IOP9 (Fig. 9d), although the low levels are not sampled as well in the control areas as in the target areas. In short, *low-level reflectivity is enhanced in the more intense convective cells during seeding in the target areas*, especially in the lee, relative to the control areas.

e. Isolating a seeding signature: Double ratio

To quantify the possible seeding impact and examine its vertical reach, we analyze what Pokharel et al. (2014) call the reflectivity impact factor (ZIP) to tease out the effect that seeding may have on reflectivity. The ZIP is a double difference that, with a suitable relationship between Z and precipitation rate R ($Z - R$), can be expressed as double precipitation ratio (e.g., Gabriel 1999). In Part I ZIP is defined relative to an *upstream* control area, but here ZIP is defined as the difference between the Z change in a target area and that in the corresponding *lateral* control area:

$$\mathrm{ZIP}_{\mathrm{Upwind}} = \Delta\mathrm{dB}Z_{\mathrm{Upwind\_Target}} - \Delta\mathrm{dB}Z_{\mathrm{Upwind\_Control}} \quad (1)$$

and

$$\mathrm{ZIP}_{\mathrm{Lee}} = \Delta\mathrm{dB}Z_{\mathrm{Lee\_Target}} - \Delta\mathrm{dB}Z_{\mathrm{Lee\_Control}}, \quad (2)$$

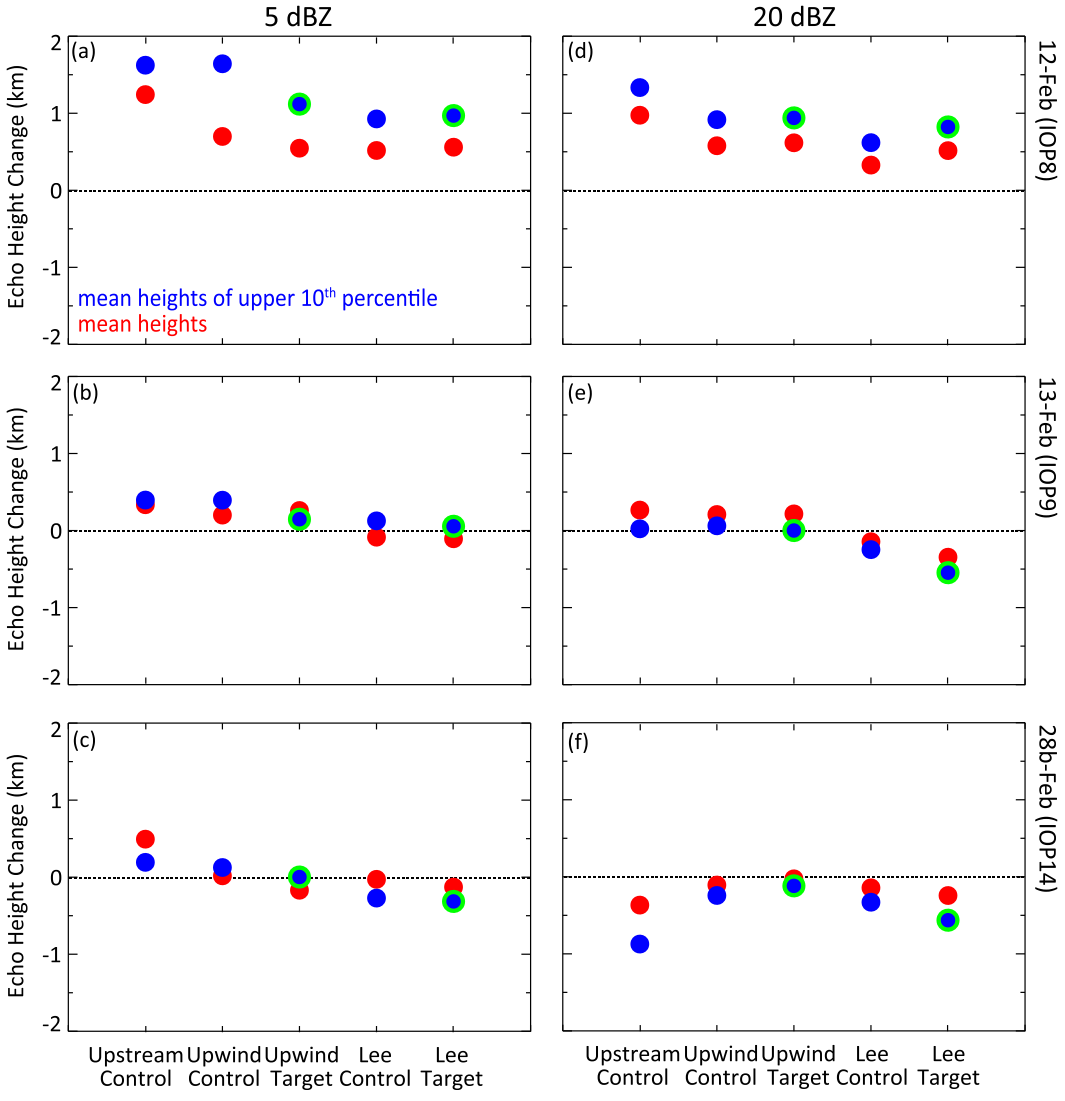

FIG. 8. The mean of all (red) and the upper 10th percentile (blue) of the change in 5- and 20-dBZ echo height (SEED − NOSEED) for the three cases. The green circles highlight indicators of a possible dynamic-seeding signal.

where $\Delta\mathrm{dB}Z = \mathrm{dB}Z_{\mathrm{SEED}} - \mathrm{dB}Z_{\mathrm{NOSEED}}$.

The ZIP is proportional to the relative change in precipitation rate in a target area in comparison with the same relative change in a control area. To show this, we first define the precipitation impact factor (PIF; Pokharel et al. 2014):

$$\mathrm{PIF} = (R_{S,T}/R_{N,T})/(R_{S,C}/R_{N,C}), \tag{3}$$

where S = SEED, N = NOSEED, T = target, and C = control. In other words, PIF is the relative change in R (SEED relative to NOSEED) in the target area in comparison with the same relative change in the control area. With a suitable Z–R relationship ($R = aZ^b$), PIF can be related to ZIP as follows:

$$\mathrm{PIF} = 10^{(b\times\mathrm{ZIP})/10}. \tag{4}$$

Matrosov et al. (2009) suggests a value of $b = 0.67$ for X-band radar in snow.

The ZIP profiles of the three IOPs are shown in Fig. 10; the solid (dashed) lines represent the upwind (lee) target area. Note that the data density decreases rapidly above ~2 km AGL (Figs. 5 and 6), especially in IOP9 and IOP14, and therefore the ZIP profiles become unrepresentative there. The main message from Fig. 10 is that, in all three IOPs, ZIP is positive below ~1 km AGL and that ZIP is larger in the lee than upwind of the crest in that shallow layer. While natural variability cannot be ruled out, especially since the sample size is small, the consistency of the three IOPs suggests a positive effect of

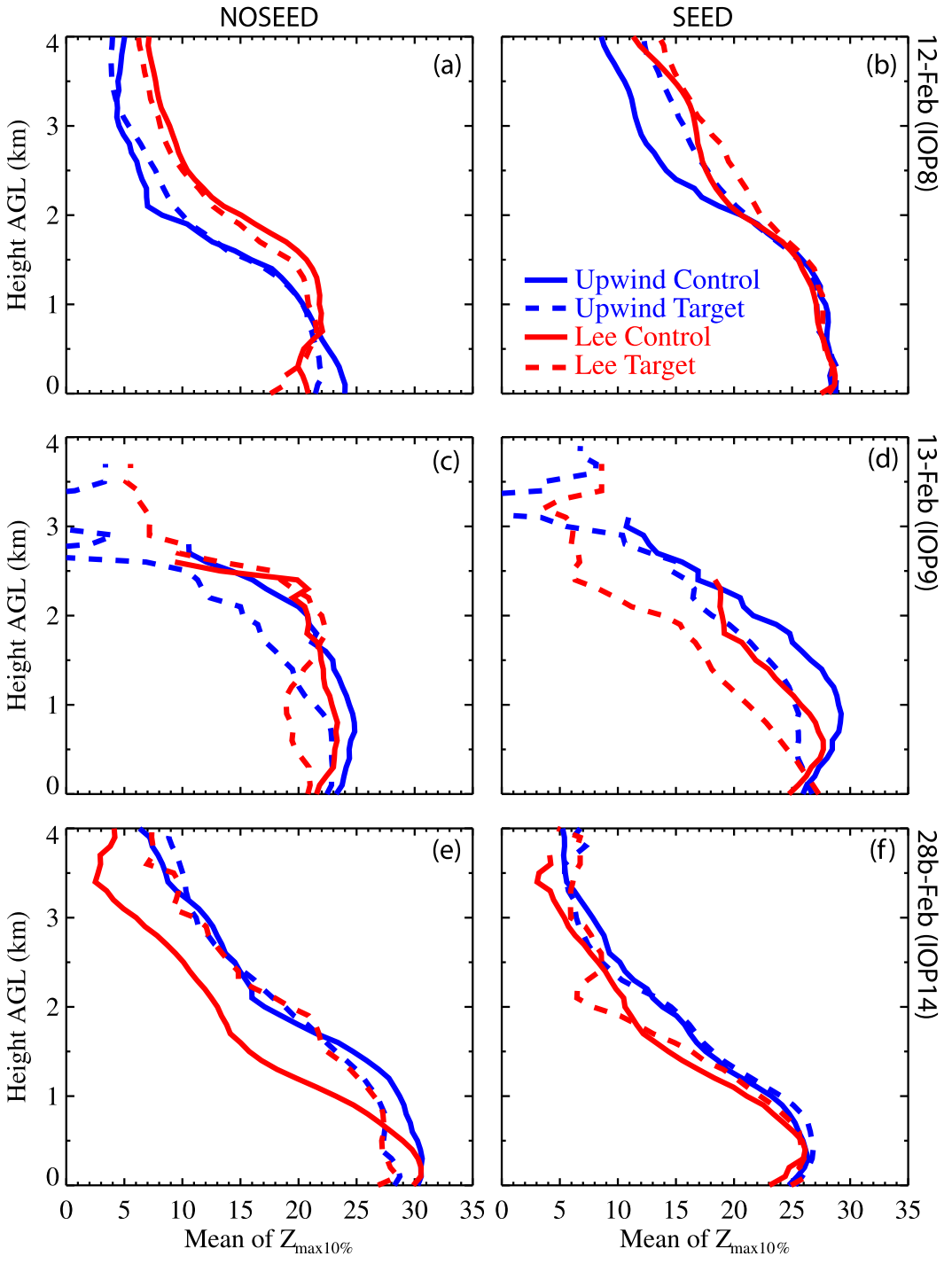

FIG. 9. The mean profiles of the upper 10th percentile of reflectivity over the five study areas for the three cases during NOSEED and SEED.

seeding on precipitation, mostly at a large distance (>~20 km) from the AgI generators. Because the seeding is ground based, any impact can be expected to be shallow. One detail is worth mentioning: the positive (negative) ZIP values above 0.8 km AGL in IOP9 on the upwind (lee) side are due to a change in flow regime, with localized plunging flow during SEED suppressing convection in the target lee (Figs. 3b,e).

We now compare ZIP profiles for the six stratiform cases analyzed in Part I and three convective cases

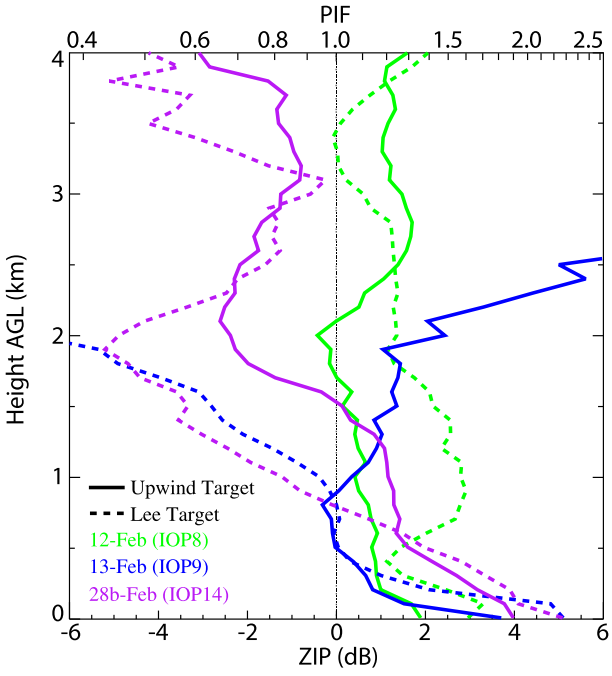

FIG. 10. Profiles of ZIP, which is defined either as the reflectivity change (SEED − NOSEED) in the upwind target region relative to the change in the upwind control region or as the change in the lee target region relative to the lee control region. The solid lines indicate the ZIP for the upwind target region, and dashed lines indicate the ZIP for the lee target region.

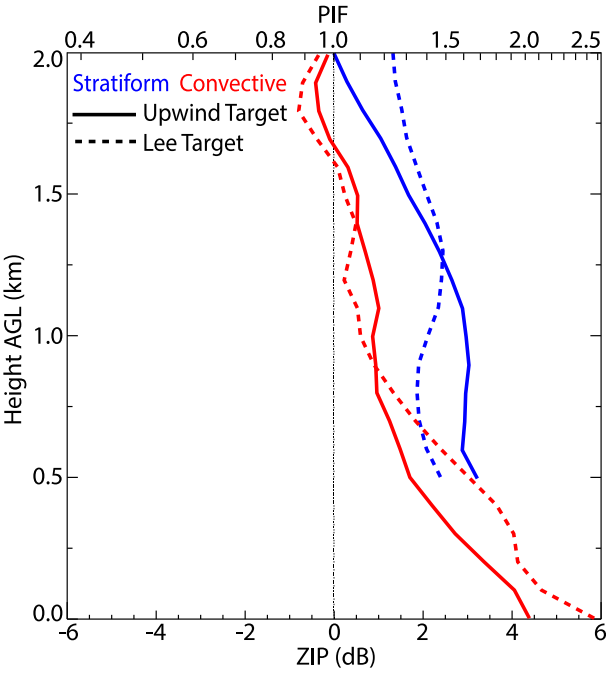

FIG. 11. Average ZIP profiles of the upwind target region (solid lines) and lee target region (dashed lines) for the six stratiform cases analyzed in Part I (blue) and the three convective cases analyzed in this paper (red).

analyzed in this paper (Fig. 11). Although the choice of control region is not the same for stratiform and convective clouds, this figure reveals an interesting difference in the distribution of the seeding impact. For the stratiform clouds, precipitation enhancement is mostly observed in the close-fetch upwind area, whereas it is more pronounced in the lee for the convective clouds. This result is consistent with spatial differences in natural precipitation: Geerts et al. (2015) analyzed 15 shallow storms over the adjacent Medicine Bow range and found that stratiform clouds usually produce more precipitation on the upwind side and quickly dry out in the lee. Convective storms tend to produce more natural precipitation in the lee, unless accelerating, plunging flow suppresses convection there. Geerts et al. (2015) hypothesize that precipitation is delayed and thus advected downwind because of convective updrafts that carry snow particles up first before the particles can settle down. Figure 11 suggests that seeding amplifies the trend for hydrometeors grown in orographic convection to become sediment in the lee.

f. Changes in snow-growth processes

The LWP was small in all three IOPs (Table 2). Flight-level measurements indicate mean liquid water content of $0.14\,g\,m^{-3}$ in IOP9 and $0.09\,g\,m^{-3}$ in IOP14 (according to Gerber Instruments AG probe measurements) both of which are small values. (There was no UWKA flight during IOP8.) The flight level was 4.0 km MSL in both flights. The mean drop sizes were 15.9 μm in IOP9 and 10.5 μm in IOP14 at flight level, according to a cloud droplet probe. This suggests that snow grows mainly by deposition (e.g., the Bergeron process) in these shallow clouds, notwithstanding the convective updrafts. Only in IOP9 was the upper-10th-percentile droplet size relatively large (25.1 μm), and therefore some rimed particles can be expected in that IOP (Wang and Ji 2000).

Ice-crystal images taken at Battle Pass with a camera show that dendrites dominate in all three IOPs. This is not surprising since the echo tops generally were just above the dendritic growth zone (~−15°C; e.g., Libbrecht 2005). One example for each IOP is included in Fig. 12. In IOP8 most dendrites had aggregated, especially during SEED (when convection was more intense). Some needles, columns, and plates were evident as well, all with very little apparent riming. Much less aggregation was present in the more shallow convection of IOP9, yielding beautiful dendrites. Some columns capped by plates were present. Many of the crystals were lightly rimed (Fig. 12h), both during NOSEED and SEED, consistent with the larger droplets observed at

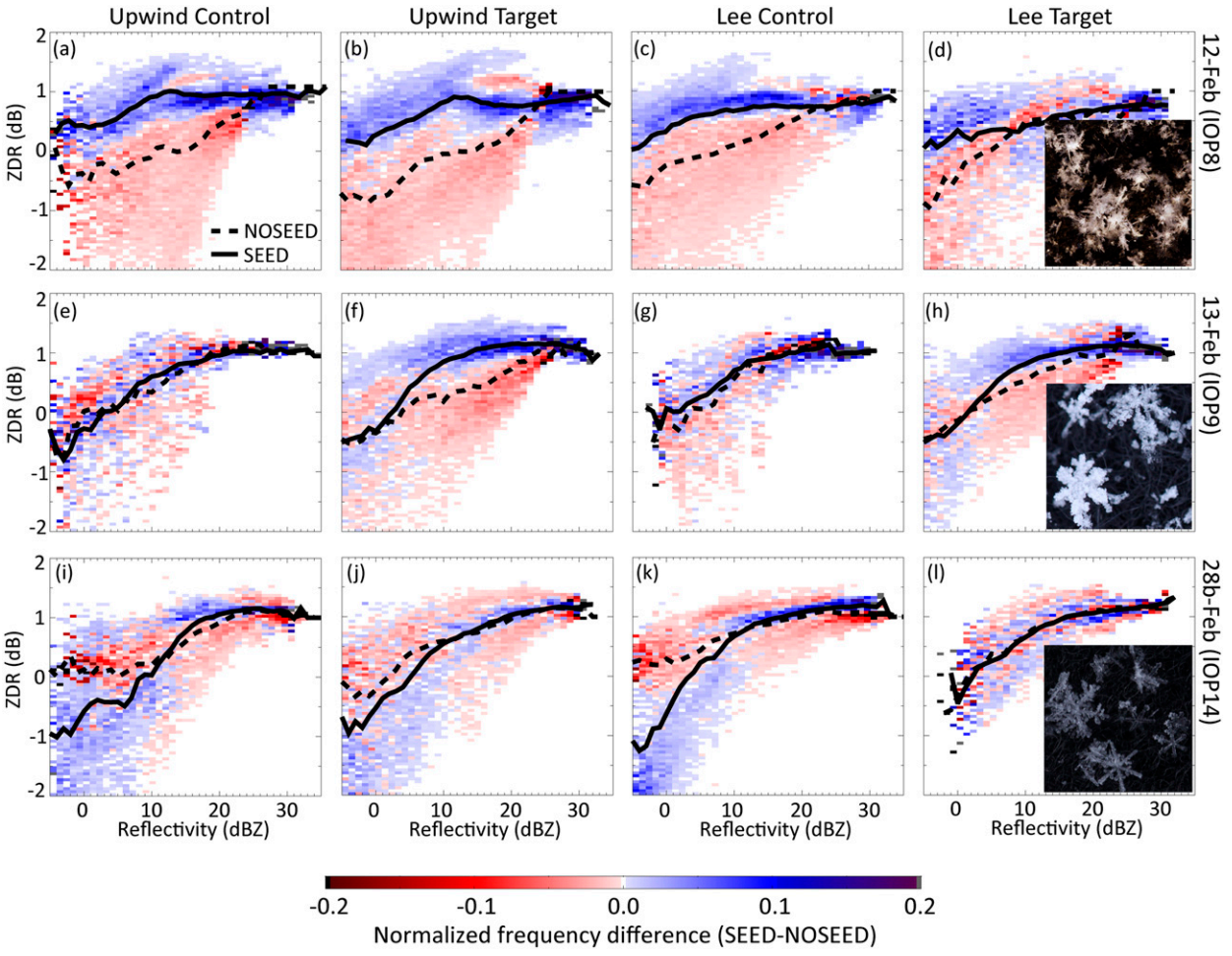

FIG. 12. Reflectivity–ZDR correlations and examples of snow-crystal photography taken during SEED for the three cases.

flight level during this IOP. More intense riming (and occasional aggregation) corresponded to the passage of a convective cell overhead.

Most crystals photographed in IOP14 were dendrites, with some needles and plates. There is some evidence of light riming and aggregation, but only during NOSEED, when convection was more intense (Figs. 9e,f). More detailed images from a cloud-particle imager (CPI; Lawson et al. 2006) were collected at Battle Pass during IOP14. Dendrites and needles prevailed during NOSEED, many of them lightly aggregated. This result indicates that ice particles were initiated between approximately −5° and −20°C, with dendrites developing in the lower end of that range. Many irregular, small ice particles were present as well, possibly because of blowing snow during IOP14, but almost no heavily aggregated or rimed particles were recorded by the CPI. CPI imagery did not substantially change during the follow-up SEED period.

In summary, the ice-crystal imagery does not reveal any significant changes from NOSEED to SEED. Observed changes can be attributed to the passage of convective cells overhead and to changes in convective intensity during the IOP.

We now examine the variation of differential reflectivity (ZDR) with Z. On average (all IOPs, all regions of interest, but only below 1.5 km AGL), ZDR values are ~0 dB at a Z value of 5 dBZ (smaller ice crystals and interstitial stratiform snowfall), and ~1 dB at 20 dBZ (larger crystals, usually in convective cells). This result has two implications. First, ice crystals tend to have their large axis near the level plane, which implies little riming. Heavily rimed particles tend to be rounder and tumble freely, resulting in a lower ZDR (e.g., Plummer et al. 2010). Second, it implies that larger particles tend to be more 2D and/or more level oriented. This increase of ZDR with Z tends to level off around 20 dBZ for the three convective cases, suggesting that graupel and large

aggregates are absent in the convective cores. If heavily rimed particles or large aggregates were present, ZDR would tend to decrease with increasing Z. Both graupel and dry aggregates tend to have a near-zero ZDR and larger Z, whereas dendrites and plates tend to have a positive ZDR (since they tend to fall horizontally) and a lower Z (Vivekanandan et al. 1999; Ryzhkov and Zrnić 2007; Thompson et al. 2014). Very similar ZDR values and a similar dependence of ZDR on Z were encountered in most stratiform cases discussed in Part I.

Seeding does not significantly alter ZDR values or the variation of ZDR with Z in the three IOPs (Fig. 12). It is clear that ZDR increases with increasing Z in all three IOPs, in all regions. This result indicates that, in all four regions, three IOPs, and seeding choices (off/on), ice crystals mainly grow by vapor deposition. Any seeding impact appears to be subtle. The similarity of the Z–ZDR relation in the target areas in the convective cores, especially in IOP14, suggests that seeding has no measurable impact on the habit or riming fraction of hydrometeors. This finding may imply that the observed low-level Z increase (Figs. 9e,f) is largely due to an increase in snow concentration rather than to snow size.

There may be some seeding-induced change in IOP9 (Fig. 12, middle row), in which some large droplets were encountered at flight level and rimed ice particles fell at Battle Pass. The ZDR values in the control areas were lower during SEED, especially for the large Z values (convective cores), suggesting more riming, probably due to increased convective activity (Fig. 8d). Yet in the target areas ZDR values in the convective cores hardly changed during SEED, suggesting that growth through the Bergeron process was sustained during SEED, even though convection was deeper. The reason for this may be an abundance of ice crystals and thus a shorter average distance from a droplet to an ice crystal, facilitating diffusional growth (e.g., Fukuta and Takahashi 1999). In fact, the ice crystal concentration was nearly an order of magnitude larger at flight level (~950 m above Battle Pass) in the target region during SEED than during NOSEED, according to data from a cloud-imaging probe and a 2D precipitation probe (Fig. 15a in Pokharel et al. 2014). Yet no such increase was seen in the upwind control region (Fig. 15b in Pokharel et al. 2014).

5. Discussion

The wintertime orographic precipitation studied here largely results from convection, sometimes embedded in shallow stratiform clouds over the mountain. This convection is triggered by potential instability released in boundary layer air lifted over the terrain, yet it remains relatively shallow, weak, and with little SLW relative to warm-season deep convection. The dynamic-seeding mechanism is not discernible in this convection, mainly because this mechanism requires a high SLW content in the cloud parcel so that enough extra latent heat can be released to raise the cloud top. In the convective clouds sampled during ASCII, however, the SLW content available for freezing is probably too low. In addition, the dynamic-seeding impact strongly depends on the stage of convection. Rosenfeld and Woodley (1993) argue that a nonseeded convective cloud goes through five stages: the cumulus growth stage, supercooled rain stage, cloud-top rainout stage (i.e., glaciation stage), downdraft stage, and dissipation stage. Only seeding clouds that can grow to the glaciation stage will have the potential of strong dynamic response. It appears to be a rare coincidence in ASCII that an orographic cloud develops at the right place downwind of the AgI generators and reaches this third stage while still upwind of the crest, because the instability is relatively low, the convection tends to collapse, and the SLW tends to evaporate in the lee. Thus probably only a few cells crossing the target area in the IOPs studied here were suitably seeded. IOP9 may be best suited because of weaker winds (Table 2). This issue is explored further in a modeling study of IOP9 (Chu et al. 2015).

In short, we have learned that the dynamic-seeding concept does not apply, or at least that it is not discernible, that the seeding impact is confined to the lowest ~1 km AGL, and that this impact is more pronounced in the lee. We emphasize, as we did in Part I, that the observed changes can be entirely natural, as the sample size (three IOPs) is small, the SEED and NOSEED periods are short, and the target and control areas are small. Low-level ZIP values may be positive in all three IOPs, but the trends in the control areas do not need to be the same as in the target areas. Yet the preponderance of evidence—from transects and maps of Z, profiles of average and convective-core Z, ZDR-versus-Z displays, and snow photography—suggests that AgI seeding increases the snowfall rate in the sampled shallow convective orographic clouds, notwithstanding the low SLW content.

6. Conclusions

The impact of ground-based glaciogenic seeding on convective winter orographic clouds is analyzed using a scanning X-band dual-polarization radar. The data were collected in the ASCII-12 campaign over the Sierra Madre in southern Wyoming. This study presents an analysis of the three IOPs with shallow to moderately

deep convection. To examine the seeding impact, five study areas are designed—three control and two target areas—and measurements from an untreated period (NOSEED) are compared with those from a treated period (SEED). The major conclusions are as follows:

- Evidence from radar reflectivity changes—including the storm evolution across the mountain, temporal differences (SEED − NOSEED), changes in the intensity of convective cells, and double differences (ZIP) in all the three IOPs—suggests a seeding-induced reflectivity increase in convective cells within the lowest 1 km, especially in the lee target area. This confirms the first hypothesis that seeding of shallow convective orographic clouds enhances snowfall at a greater fetch when compared with stratiform clouds (studied in Part I). The response to seeding likely is delayed because of deeper mixing in convective orographic clouds: seeding-impacted ice particles thus are advected farther downwind before they can settle down.
- The radar echo-top heights are not higher during seeding in the target areas than in the control areas. This confirms the second hypothesis that these shallow, benign, and cold-based convective clouds do not contain enough liquid water for the dynamic-seeding mechanism to be relevant.
- ZDR–Z relations and snow photography indicate that snow grows mainly by diffusion and aggregation and not by riming and that the ice crystals are mainly dendritic. This process is not substantially altered by seeding.

We emphasize that these findings are based on a small sample size of three IOPs and thus are not conclusive in terms of the impact of glaciogenic seeding on shallow orographic convective clouds. More field observations coupled with numerical simulations are needed to further explore the microphysical ''chain of events'' resulting from the injection of glaciogenic nuclei in orographic clouds. This study unambiguously shows that X-band dual-polarization radar can be a powerful tool to examine the impact of artificial (or natural) seeding on microphysical processes.

Acknowledgments. The ASCII campaign was funded by National Science Foundation Grant AGS-1058426. The DOW is an NSF Lower Atmospheric Observing Facility supported by NSF Grant NSF-1361237. This work also received funding from the Wyoming Water Development Commission and the U.S. Geological Survey, under the auspices of the University of Wyoming Water Research Program. The operation of the AgI generators and microwave radiometer was supported by the Wyoming Weather Modification Pilot Project, which was funded by the Wyoming government. The dedication of the DOW crew under harsh weather conditions at Battle Pass during ASCII is much appreciated. The ice-crystal photography was done by Yang Yang. This work benefitted from discussions with and assistance from Binod Pokharel of the University of Wyoming and Katja Friedrich and Joshua Aikins of the University of Colorado.

REFERENCES

Breed, D., R. Rasmussen, C. Weeks, B. Boe, and T. Deshler, 2014: Evaluating winter orographic cloud seeding: Design of the Wyoming Weather Modification Pilot Project (WWMPP). *J. Appl. Meteor. Climatol.*, **53**, 282–299, doi:10.1175/JAMC-D-13-0128.1.

Bruintjes, R. T., 1999: A review of cloud seeding experiments to enhance precipitation and some new prospects. *Bull. Amer. Meteor. Soc.*, **80**, 805–820, doi:10.1175/1520-0477(1999)080<0805:AROCSE>2.0.CO;2.

Chu, X., L. Xue, B. Geerts, R. Rasmussen, and D. Breed, 2014: A case study of radar observations and WRF LES simulations of the impact of ground-based glaciogenic seeding on orographic clouds and precipitation. Part I: Observations and model validations. *J. Appl. Meteor. Climatol.*, **53**, 2264–2286, doi:10.1175/JAMC-D-14-0017.1.

——, B. Geerts, and L. Xue, 2015: Cloud-resolving large eddy simulations of the impact of ground-based glaciogenic seeding on shallow convective orographic clouds and precipitation. *20th Conf. on Planned and Inadvertent Weather Modification*, Phoenix, AZ, Amer. Meteor. Soc., 5.4. [Available online at https://ams.confex.com/ams/95Annual/webprogram/Paper267584.html.]

Freud, E., H. Koussevitzky, T. Goren, and D. Rosenfeld, 2015: Cloud microphysical background for the Israel-4 cloud seeding experiment. *Atmos. Res.*, **158–159**, 122–138, doi:10.1016/j.atmosres.2015.02.007.

Fukuta, N., and T. Takahashi, 1999: The growth of atmospheric ice crystals: A summary of findings in vertical supercooled cloud tunnel studies. *J. Atmos. Sci.*, **56**, 1963–1979, doi:10.1175/1520-0469(1999)056<1963:TGOAIC>2.0.CO;2.

Gabriel, K. R., 1999: Ratio statistics for randomized experiments in precipitation stimulation. *J. Appl. Meteor.*, **38**, 290–301, doi:10.1175/1520-0450(1999)038<0290:RSFREI>2.0.CO;2.

Gagin, A., and J. Neumann, 1981: The second Israeli randomized cloud seeding experiment: Evaluation of the results. *J. Appl. Meteor.*, **20**, 1301–1311, doi:10.1175/1520-0450(1981)020<1301:TSIRCS>2.0.CO;2.

——, D. Rosenfeld, and R. E. Lopez, 1985: The relationship between height and precipitation characteristics of summertime convective cells in south Florida. *J. Atmos. Sci.*, **42**, 84–94, doi:10.1175/1520-0469(1985)042<0084:TRBHAP>2.0.CO;2.

Geerts, B., Q. Miao, Y. Yang, R. Rasmussen, and D. Breed, 2010: An airborne profiling radar study of the impact of glaciogenic cloud seeding on snowfall from winter orographic clouds. *J. Atmos. Sci.*, **67**, 3286–3301, doi:10.1175/2010JAS3496.1.

——, and Coauthors, 2013: The AgI Seeding Cloud Impact Investigation (ASCII) campaign 2012: Overview and preliminary results. *J. Wea. Modif.*, **45**, 24–43.

——, Y. Yang, R. Rasmussen, S. Haimov, and B. Pokharel, 2015: Snow growth and transport patterns in orographic storms as estimated from airborne vertical-plane dual-Doppler radar data. *Mon. Wea. Rev.*, **143**, 644–665, doi:10.1175/MWR-D-14-00199.1.

Grant, L. O., and R. E. Elliott, 1974: The cloud seeding temperature window. *J. Appl. Meteor.*, **13**, 355–363, doi:10.1175/1520-0450(1974)013<0355:TCSTW>2.0.CO;2.

Hallet, J., 1981: Ice crystal evolution in Florida summer cumuli following AgI seeding. Preprints, *Eighth Conf. on Inadvertent and Planned Weather Modification*, Reno, NV, Amer. Meteor. Soc., 114–115.

Hashimoto, A., T. Kato, S. Hayashi, and M. Murakami, 2008: Seedability assessment for winter orographic snow clouds over the Echigo Mountains. *SOLA*, **4**, 69–72, doi:10.2151/sola.2008-018.

Holroyd, E. W., J. T. McPartland, and A. B. Super, 1988: Observation of silver iodide plumes over the Grand Mesa of Colorado. *J. Appl. Meteor.*, **27**, 1125–1144, doi:10.1175/1520-0450(1988)027<1125:OOSIPO>2.0.CO;2.

Huggins, A. W., 2007: Another wintertime cloud seeding case study with strong evidence of seeding effects. *J. Wea. Modif.*, **39**, 9–36.

Isaac, G. A., R. S. Schemenauer, C. L. Crozier, A. J. Chisholm, J. I. Macpherson, N. R. Bobbitt, and L. B. Machattie, 1977: Preliminary tests of a cumulus cloud seeding technique. *J. Appl. Meteor.*, **16**, 949–958, doi:10.1175/1520-0450(1977)016<0949:PTOACC>2.0.CO;2.

——, J. W. Strapp, R. S. Schemenauer, and J. I. Macpherson, 1982: Summer cumulus cloud seeding experiments near Yellowknife and Thunder Bay, Canada. *J. Appl. Meteor.*, **21**, 1266–1285, doi:10.1175/1520-0450(1982)021<1266:SCCSEN>2.0.CO;2.

Jing, X., B. Geerts, and K. Friedrich, 2015: Dual-polarization radar data analysis of the impact of ground-based glaciogenic seeding on winter orographic clouds. Part I: Mostly stratiform clouds. *J. Appl. Meteor. Climatol.*, **54**, 1945–1970, doi:10.1175/JAMC-D-14-0257.1.

Lawson, P., B. A. Baker, P. Zmarzly, D. O'Connor, Q. Mo, J.-F. Gayet, and V. Shcherbakov, 2006: Microphysical and optical properties of atmospheric ice crystals at South Pole Station. *J. Appl. Meteor. Climatol.*, **45**, 1505–1524, doi:10.1175/JAM2421.1.

Libbrecht, K. G., 2005: The physics of snow crystals. *Rep. Prog. Phys.*, **68**, 855–895, doi:10.1088/0034-4885/68/4/R03.

Manton, M. J., L. Warren, S. L. Kenyon, A. D. Peace, S. P. Bilish, and K. Kemsley, 2011: A confirmatory snowfall enhancement project in the Snowy Mountains of Australia. Part I: Project design and response variables. *J. Appl. Meteor. Climatol.*, **50**, 1432–1447, doi:10.1175/2011JAMC2659.1.

Matrosov, S. Y., C. Campbell, D. Kingsmill, and E. Sukovich, 2009: Assessing snowfall rates from X-band radar reflectivity measurements. *J. Atmos. Oceanic Technol.*, **26**, 2324–2339, doi:10.1175/2009JTECHA1238.1.

Orville, H. D., 1996: A review of cloud modeling in weather modification. *Bull. Amer. Meteor. Soc.*, **77**, 1535–1555, doi:10.1175/1520-0477(1996)077<1535:AROCMI>2.0.CO;2.

Plummer, D. M., S. Göke, R. M. Rauber, and L. D. Girolamo, 2010: Discrimination of mixed- versus ice-phase clouds using dual-polarization radar with application to detection of aircraft icing regions. *J. Appl. Meteor. Climatol.*, **49**, 920–936, doi:10.1175/2009JAMC2267.1.

Pokharel, B., B. Geerts, X. Jing, K. Friedrich, J. Aikins, D. Breed, R. Rasmussen, and A. Huggins, 2014: The impact of ground-based glaciogenic seeding on clouds and precipitation over mountains: A multi-sensor case study of shallow precipitating orographic cumuli. *Atmos. Res.*, **147–148**, 162–182, doi:10.1016/j.atmosres.2014.05.014.

——, ——, and ——, 2015a: The impact of ground-based glaciogenic seeding on clouds and precipitation over mountains: A case study of a shallow orographic cloud with large supercooled droplets. *J. Geophys. Res. Atmos.*, **120**, 6056–6079, doi:10.1002/2014JD022693.

Rangno, A. L., and P. V. Hobbs, 1995: A new look at the Israeli cloud seeding experiments. *J. Appl. Meteor.*, **34**, 1169–1193, doi:10.1175/1520-0450(1995)034<1169:ANLATI>2.0.CO;2.

Rosenfeld, D., and W. L. Woodley, 1989: Effects of cloud seeding in west Texas. *J. Appl. Meteor.*, **28**, 1050–1080, doi:10.1175/1520-0450(1989)028<1050:EOCSIW>2.0.CO;2.

——, and ——, 1993: Effects of cloud seeding in west Texas: Additional results and new insights. *J. Appl. Meteor.*, **32**, 1848–1866, doi:10.1175/1520-0450(1993)032<1848:EOCSIW>2.0.CO;2.

Ryan, B. F., and W. D. King, 1997: A critical review of the Australian experience in cloud seeding. *Bull. Amer. Meteor. Soc.*, **78**, 239–254, doi:10.1175/1520-0477(1997)078<0239:ACROTA>2.0.CO;2.

Ryzhkov, A. V., and D. S. Zrnić, 2007: Depolarization in ice crystals and its effect on radar polarimetric measurements. *J. Atmos. Oceanic Technol.*, **24**, 1256–1267, doi:10.1175/JTECH2034.1.

Sax, R. I., J. Thomas, M. Bonebrake, and J. Hallett, 1979: Ice evolution within seeded and nonseeded Florida cumuli. *J. Appl. Meteor.*, **18**, 203–214, doi:10.1175/1520-0450(1979)018<0203:IEWSAN>2.0.CO;2.

Simpson, J., and W. L. Woodley, 1971: Seeding cumulus in Florida: New 1970 results. *Science*, **172**, 117–126, doi:10.1126/science.172.3979.117.

——, G. W. Brier, and R. H. Simpson, 1967: Stormfury cumulus seeding experiment 1965: Statistical analysis and main results. *J. Atmos. Sci.*, **24**, 508–521, doi:10.1175/1520-0469(1967)024<0508:SCSESA>2.0.CO;2.

Smith, P. L., and Coauthors, 1984: HIPLEX-1: Experimental design and response variables. *J. Climate Appl. Meteor.*, **23**, 497–512, doi:10.1175/1520-0450(1984)023<0497:HEDARV>2.0.CO;2.

Thompson, E. J., S. A. Rutledge, B. Dolan, V. Chandrasekar, and B. L. Cheong, 2014: A dual-polarization radar hydrometeor classification algorithm for winter precipitation. *J. Atmos. Oceanic Technol.*, **31**, 1457–1481, doi:10.1175/JTECH-D-13-00119.1.

Vali, G., L. R. Koenig, and T. C. Yoksas, 1988: Estimate of precipitation enhancement potential for the Duero basin of Spain. *J. Appl. Meteor.*, **27**, 829–850, doi:10.1175/1520-0450(1988)027<0829:EOPEPF>2.0.CO;2.

Vivekanandan, J., S. M. Ellis, R. Oye, D. S. Zrnić, A. V. Ryzhkov, and J. Straka, 1999: Cloud microphysics retrieval using S-band dual-polarization radar measurements. *Bull. Amer. Meteor. Soc.*, **80**, 381–388, doi:10.1175/1520-0477(1999)080<0381:CMRUSB>2.0.CO;2.

Wang, P. K., and W. Ji, 2000: Collision efficiencies of ice crystals at low-intermediate Reynolds numbers colliding with supercooled cloud droplets: A numerical study. *J. Atmos. Sci.*, **57**, 1001–1009, doi:10.1175/1520-0469(2000)057<1001:CEOICA>2.0.CO;2.

World Meteorological Organization, 1986: Synopsis of the WMO Precipitation Enhancement Project—1985. Precipitation Enhancement Project Rep. 34, 97 pp.

Woodley, W. L., J. Jordan, J. Simpson, R. Biondini, J. A. Flueck, and A. Barnston, 1982: Rainfall results of the Florida Area Cumulus Experiment, 1970–76. *J. Appl. Meteor.*, **21**, 139–164, doi:10.1175/1520-0450(1982)021<0139:RROTFA>2.0.CO;2.

Yuter, S. E., and R. A. Houze Jr., 1995: Three-dimensional kinematic and microphysical evolution of Florida cumulonimbus. Part II: Frequency distributions of vertical velocity, reflectivity, and differential reflectivity. *Mon. Wea. Rev.*, **123**, 1941–1963, doi:10.1175/1520-0493(1995)123<1941:TDKAME>2.0.CO;2.